

Contents lists available at ScienceDirect

# Optik

journal homepage: www.elsevier.com/locate/ijleo



### Original research article

# Chiral metasurfaces of wavy rectangle resonators with tunable circular dichroism



Xiangkai Zeng <sup>a</sup>, Daniel Rosenmann <sup>b</sup>, David A. Czaplewski <sup>b</sup>, Jie Gao <sup>a, c, \*</sup>, Xiaodong Yang <sup>a, \*\*</sup>

- <sup>a</sup> Department of Mechanical and Aerospace Engineering, Missouri University of Science and Technology, Rolla, MO 65409, USA
- <sup>b</sup> Center for Nanoscale Materials, Argonne National Laboratory, Lemont, IL 60439, USA
- <sup>c</sup> Department of Mechanical Engineering, Stony Brook University, Stony Brook, NY 11794, USA

#### ARTICLE INFO

#### ABSTRACT

Keywords: Mid-infrared range Chiral metasurface Circular dichroism Chiral metasurfaces operating at the mid-infrared frequencies are of great interest for chiral molecule vibrational sensing and other applications. Here, mid-infrared chiral metasurfaces of wavy rectangle resonators with strong chiroptical response and tunable circular dichroism (CD) are demonstrated. The chiral metasurface exhibits a high CD value of more than 0.57 as the chiral plasmonic resonance wavelength is tuned from 4.96 to 5.82  $\mu m$  by enlarging the geometric dimensions of the unit cell. Furthermore, CD values can be continuously tuned from positive to zero and negative without altering the chiral plasmonic resonance wavelength, by simply relocating the cutting slot to change the geometric symmetry of the wavy rectangle structure. These results aim to advance the development of many promising applications in mid-infrared frequencies including protein molecule detection, thermal emission control, and infrared-light communication.

#### 1. Introduction

Chiral metamaterials are artificial structures exhibiting unique circular dichroism responses due to their symmetry-breaking features [1,2], which interact differently with left- and right-handed circularly polarized (LCP and RCP) incident light [3,4]. The geometric structures of the unit cells in chiral metamaterials play a crucial role in determining their chiroptical responses such as negative refraction [5–7], circular dichroism [8–10], and optical activity [11]. According to the material selection, all-metallic, all-dielectric and metal-dielectric chiral metamaterials have been designed in the past [12–14]. In particular, metal-dielectric-metal chiral metamaterials have been extensively studied from visible, near-infrared to mid-infrared frequencies [15–22] with enhanced chiroptical properties. In the mid-infrared frequency range, chiral metamaterials show significant promise for many applications such as circular-polarization-sensitive photodetection [23], optical sensing [24–26], nonlinear optics [26], and telecommunication [27]. On the other hand, the mid-infrared range is of particular interest in molecular sensing because various vibrational modes of molecule bonds such as the carbon-oxygen bond, the alkene bond and the amide bond are located in this frequency range.

Recently, metamaterials have been utilized to enhance the plasmonic excitations of the targeted molecules through concentrated

E-mail addresses: jie.gao.5@stonybrook.edu (J. Gao), yangxia@mst.edu (X. Yang).

<sup>\*</sup> Corresponding author at: Department of Mechanical and Aerospace Engineering, Missouri University of Science and Technology, Rolla, MO 65409, USA.

<sup>\*\*</sup> Corresponding author.

near fields to reach the sensing limit for the detection of binding events in a single molecule [28–30]. This unique advantage of metamaterials can be further extended into chiral molecular sensing by designing chiral metamaterials with asymmetric structures, which enable strong chiroptical interactions between chiral molecules and superchiral near fields [31]. Chiral molecules usually have very weak chiroptical responses due to the small difference between their refractive indices under the LCP and RCP illumination, which is related to their weak molecular polarizability [32]. In contrast, chiral metamaterials with artificially designed asymmetric structures can possess much stronger chiroptical responses. This feature will considerably enhance the CD signal of chiral molecules, which could potentially decrease the data acquisition time and allow for the use of lower analyte concentrations in chiral sensing applications [33].

In this work, a unique type of mid-infrared metal-dielectric-metal chiral metasurface consisting of wavy rectangle resonators are designed and demonstrated with strong chiroptical response and tunable CD. The fundamental mechanism of circular polarization-sensitive optical absorption from the designed metasurface is elaborated using numerically simulated electromagnetic field distributions of the chiral resonant modes. As demonstrated in experiment, the chiral metasurface exhibits a high CD value of 0.62 at the chiral plasmonic resonance wavelength of 4.96 µm. By enlarging the geometric dimensions of the unit cell, the chiral plasmonic resonance wavelength is tuned from 4.96 to 5.82 µm, while the high CD value of more than 0.57 is maintained. Meanwhile, CD values are continuously tunable from positive to zero and negative at the unchanged chiral plasmonic resonance wavelength, by only varying the cutting slot location to change the geometric symmetry of the wavy rectangle structure. In comparison to the previously reported metal-dielectric-metal chiral metasurfaces with other structures like the coupled rectangle bars [16], the F-shaped structure [20], and the S-shaped structure [34] where the CD values cannot be tuned easily, the wavy rectangle structure offers the exceptional capability in flexible CD tunability and precise control of chiroptical responses for chiral metasurfaces. These results will open many new opportunities for the advancement of applications in mid-infrared frequencies such as protein molecule detection, thermal radiation control, and infrared-light communication.

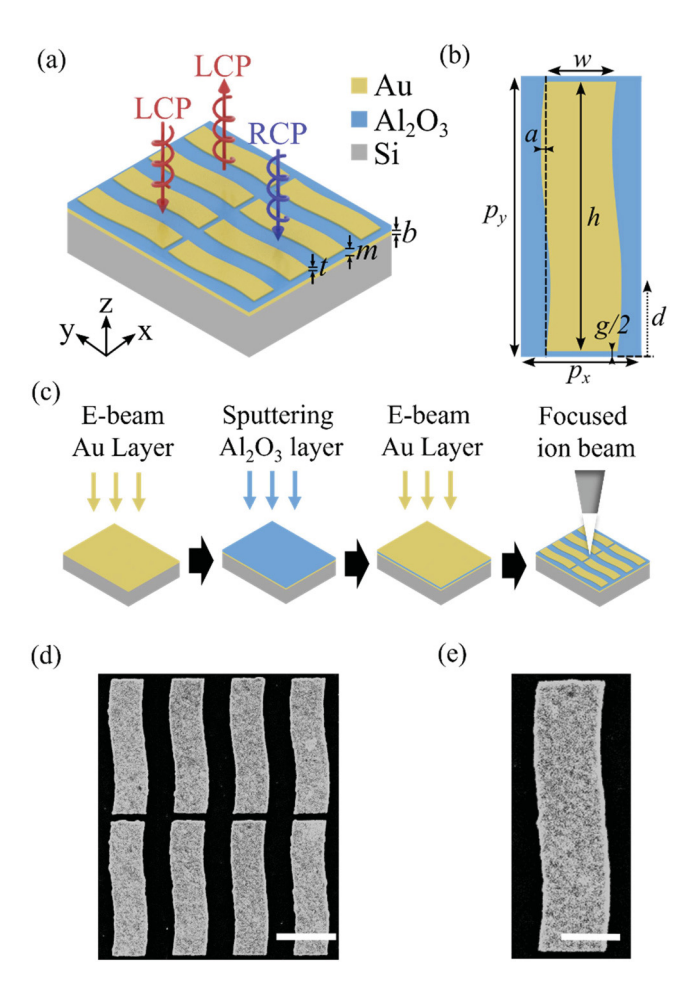
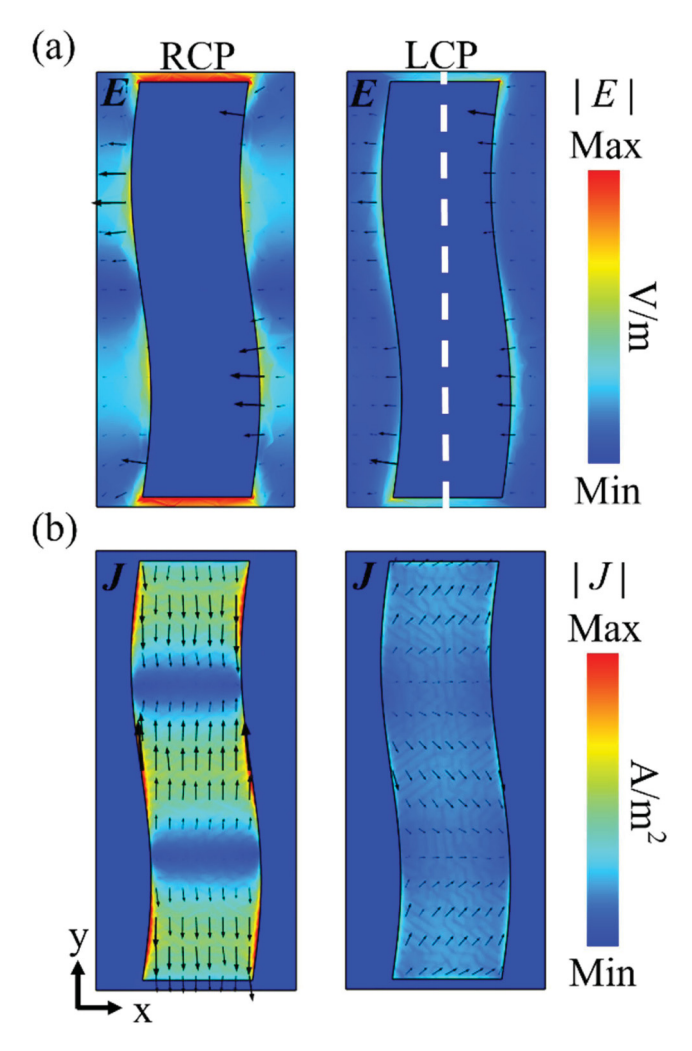


Fig. 1. (a) Diagram of the chiral metasurface consisting of wavy rectangle resonators. (b) Top-view diagram of the metasurface unit cell marked with the geometric dimensions. (c) Schematic diagram of the fabrication process of chiral metasurface. (d) Top-view SEM image of the metasurface device. Scale bar:  $2 \mu m$ . (e) Zoomed-in SEM image of the metasurface unit cell. Scale bar:  $1 \mu m$ .

#### 2. Chiral metasurface design and characterization

Fig. 1(a) illustrates the diagram of the designed metal-dielectric-metal chiral metasurface composed of a three-layer thin film of gold (Au) and alumina (Al<sub>2</sub>O<sub>3</sub>). The device consists of the wavy rectangle structures etched in the top Au layer with the thickness of t =65 nm, the middle  $Al_2O_3$  dielectric spacer with the thickness of m = 250 nm, and the bottom Au mirror layer with the thickness of b = 250 nm, and the bottom Au mirror layer with the thickness of b = 250 nm, and the bottom Au mirror layer with the thickness of b = 250 nm, and the bottom Au mirror layer with the thickness of b = 250 nm, and the bottom Au mirror layer with the thickness of b = 250 nm, and the bottom Au mirror layer with the thickness of b = 250 nm, and the bottom Au mirror layer with the thickness of b = 250 nm, and the bottom Au mirror layer with the thickness of b = 250 nm, and the bottom Au mirror layer with the thickness of b = 250 nm, and the bottom Au mirror layer with the thickness of b = 250 nm, and the bottom Au mirror layer with the thickness of b = 250 nm, and the bottom Au mirror layer with the thickness of b = 250 nm, and the bottom Au mirror layer with the thickness of b = 250 nm, and the bottom Au mirror layer with the thickness of b = 250 nm, and b = 250 nm, 200 nm. Fig. 1(b) presents the dimensions of the wavy rectangle resonator in the design, where the unit cell periods are  $p_x = 2 \mu m$  and  $p_y = 4.8 \, \mu \text{m}$ . The wavy rectangle structure is formed by inserting periodic horizontal cutting slots into a continuous sine wave slab with a period of  $p_y$ , where the sine wave border of the wavy rectangle structure follows a function of  $f(y) = a \bullet \sin\left(2\pi \bullet \frac{y+d}{p_y}\right)$ , with the sine wave amplitude a = 100 nm and the vertical shift of the cutting slot d. The gap size of the cutting slot is g = 200 nm, while the wavy rectangle structure has the dimensions of width  $w = 1.1 \, \mu m$  and length  $h = 4.6 \, \mu m$ . The vertical shift of the cutting slot d can be adjusted from 0 to  $p_y/2$  along the y direction to vary the degree of symmetry breaking for the wavy rectangle structure, so that the metasurface chiroptical response can be continuously tuned. At d=0 and  $d=p_{\gamma}/2$ , the degree of symmetry breaking for the structure is the largest to get the maximum CD responses but with the opposite CD values, while at  $d = p_v/4$ , the wavy rectangle structure has a symmetric geometry to reach a zero CD value. The cutting slot is initially set at the position of d = 0. In the design, the geometric dimensions of the metasurface unit cell, especially the sine wave amplitude a and the rectangle width w are optimized to maximize the metasurface CD response. Fig. 1(c) shows the schematic diagram of the fabrication process of chiral metasurface. First, the bottom Au layer is deposited on a silicon wafer by utilizing an electron beam evaporator (Lesker PVD250). Then, the middle Al<sub>2</sub>O<sub>3</sub> layer is deposited by a sputtering system (Lesker CMS18), followed by the deposition of the top Au layer with the electron beam evaporator. Finally, the wavy rectangle structures are formed by milling the top Au layer with a focused ion beam system (FEI Helios Nanolab 600,



**Fig. 2.** (a) Distributions of electric field |E| (color map) and electric field vector E (black arrows) at the plane of z = 460 nm for RCP and LCP incident light at the wavelength of 4.98 μm. The white dashed line marks the position of x = 1000 nm. (b) Distributions of current density |J| (color map) and current density vector J (black arrows) at the plane of z = 460 nm.

voltage 30 kV, beam current 97 pA). Fig. 1(d) displays a top-view scanning electron microscope (SEM) image of the fabricated metasurface device, while a zoomed-in SEM image of the metasurface unit cell is presented in Fig. 1(e).

The CD response in the chiral metasurface is explained through numerically simulated electromagnetic field distributions of the chiral resonant modes under RCP and LCP incidence using the COMSOL Multiphysics software. The wave excitation port is applied along the z direction with a perfectly matched layer to reduce the boundary reflection, while periodic boundary conditions are used in the x and y boundaries. In the simulation, the  $Al_2O_3$  permittivity is taken from a reference [35] and the Au permittivity is taken from the Lorentz-Drude model [36]. Fig. 2(a) illustrates the electric field distributions in the plane of z = 460 nm which is located within the top Au layer for RCP and LCP incidence at the chiral plasmonic resonance wavelength of 4.98 µm. It demonstrates that the chiral resonant mode of the wavy rectangle resonator is strongly coupled with the RCP light. It is shown that the electric field is predominantly concentrated inside the cutting slot area between the wavy rectangle structures, resulting in a high absorption of the RCP light. In contrast, the electric field generated by the LCP light is significantly weaker as the LCP light is not coupled well with the wavy rectangle resonator, so that there is a low absorption. To provide additional insight into the differential absorption of the chiral metasurface, the current density distributions in the plane of z = 460 nm for RCP and LCP light are further plotted in Fig. 2(b). It indicates that the current density created by the RCP light strongly oscillates in the y direction within the wavy rectangle structure. This gives rise to three current loops circulating around the Al<sub>2</sub>O<sub>3</sub> spacer, resulting in strong optical absorption for RCP light. However, the current density generated by the LCP light is much weaker, which leads to a low absorption. In addition, Fig. 3(a) illustrates the magnetic field distributions in the plane of z = 325 nm across the middle of the  $Al_2O_3$  spacer. It reveals that three dominant magnetic dipole modes are excited by the RCP light inside the Al<sub>2</sub>O<sub>3</sub> spacer in the x direction, corresponding to the three current loops. In contrast, one much weaker magnetic dipole mode is generated by the LCP light. Fig. 3(b) further plots the Poynting vector distributions in the plane of z = 325 nm. It shows that the power flow of RCP light is coupled well in the Al<sub>2</sub>O<sub>3</sub> spacer with three strong energy flux

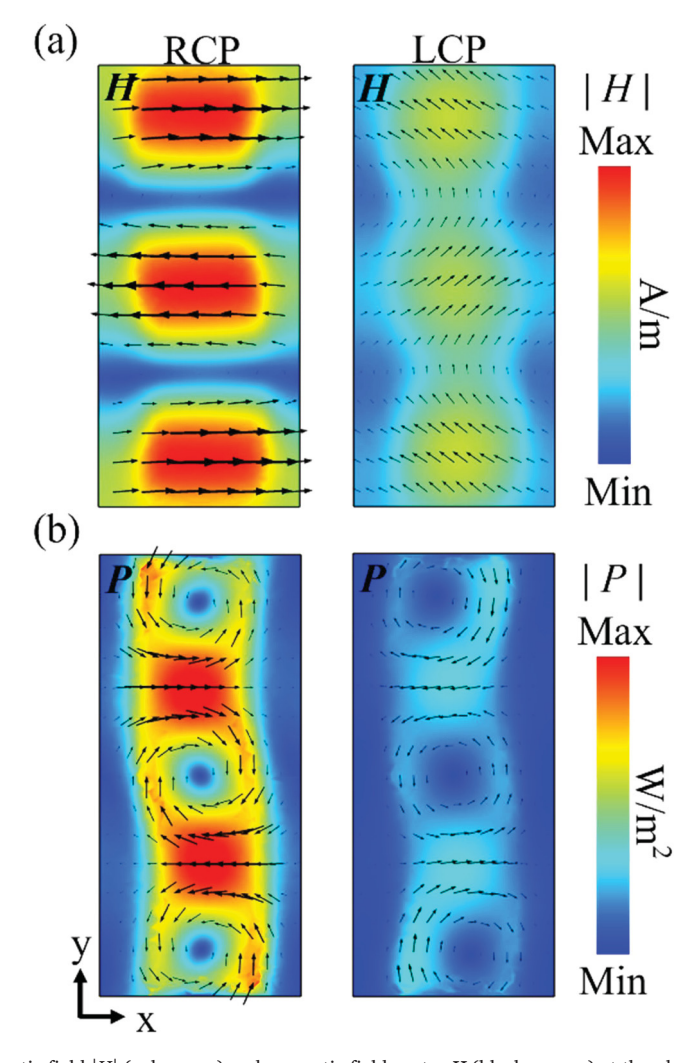
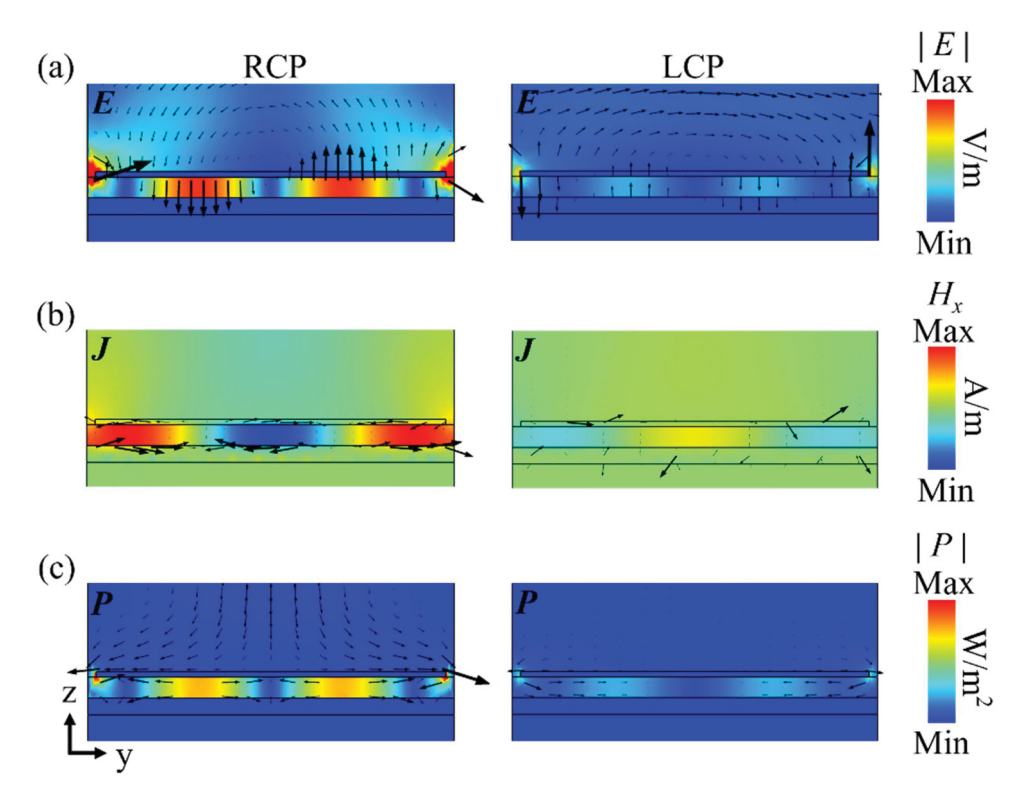


Fig. 3. (a) Distributions of magnetic field |H| (color map) and magnetic field vector H (black arrows) at the plane of z=325 nm for RCP and LCP incident light. (b) Distributions of Poynting vector |P| (color map) and P (black arrows) at the plane of z=325 nm.

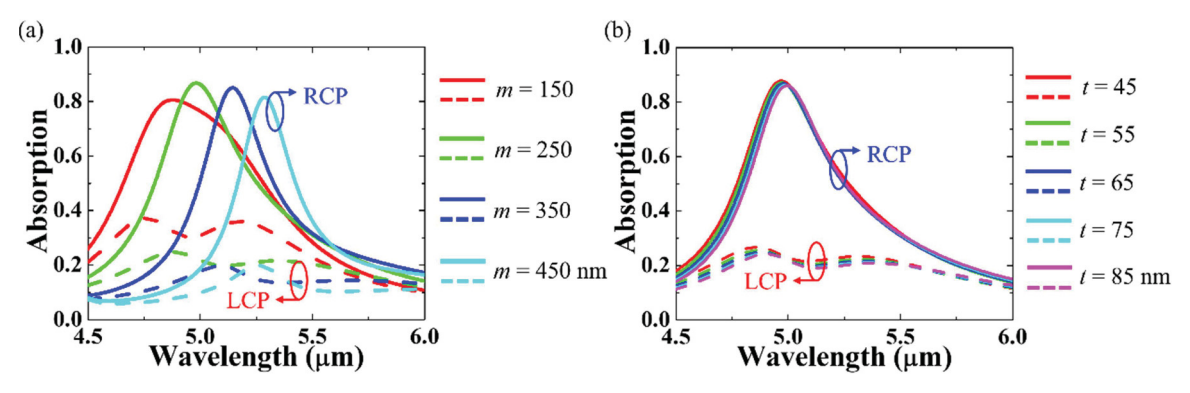
loops, but the coupled power flow from LCP light exhibits a much weaker energy flux.

Fig. 4 further shows the electromagnetic field distributions in the plane of x=1000 nm of the metasurface coupled with the RCP and LCP light, where the position of this plane is labeled in Fig. 2(a). Fig. 4(a) demonstrates that the intense electric field surrounding the Au wavy rectangle structure exists for RCP light, whereas the electric field for LCP light is very weak. Fig. 4(b) indicates that the dielectric spacer contains three strong magnetic dipole modes for RCP light, which generate current loops circulating between the top and bottom Au layers. In contrast, there is no clear magnetic dipole mode supported in the dielectric spacer for LCP light. The Poynting vector in Fig. 4(c) further demonstrates that the power flow of RCP light is effectively coupled inside the dielectric spacer to give a high absorption, but the power flow of LCP light merely propagates into the structure and most of the energy is reflected back. The large differential absorption of RCP and LCP light by the metasurface originates from the strong chiroptical interaction between the metasurface and the RCP incident light through the excitation of magnetic dipole modes together with the generated current loops within the wavy rectangle resonator. The transmission through the thick Au bottom layer is negligible, so that the absorption A is obtained from the reflection R by A=1-R. The CD value in term of absorption is then obtained by CD =  $A_{RCP}-A_{LCP}$ . For the simulated chiral metasurface, the CD value is 0.65 at the chiral plasmonic resonance wavelength of 4.98 µm, with the RCP and LCP optical absorption of  $A_{RCP}=0.86$  and  $A_{LCP}=0.21$ .

Fig. 5 shows the simulated absorption spectra of the chiral metasurfaces by considering different thicknesses of the middle  $Al_2O_3$  layer and the top Au layer. In Fig. 5(a), as the thickness m of the middle  $Al_2O_3$  layer increases from 150 to 450 nm while the thickness t of the top Au layer is fixed at t=65 nm, the resonance wavelength has a redshift from 4.88 to 5.29  $\mu$ m. The CD value also changes with the thickness m, and the maximum CD value of 0.65 is obtained at the resonance wavelength of 4.98  $\mu$ m with m=250 nm. In Fig. 5(b), as the thickness t of the top Au layer varies from 45 to 85 nm with a fixed m=250 nm, the resonance wavelength and the CD value remain approximately unchanged at 4.98  $\mu$ m and 0.65, respectively. Thus, the thicknesses of t=65 nm and m=250 nm are selected in the current chiral metasurface design. The chiral plasmonic resonance of the metasurface can be tuned through linearly enlarging the geometric parameters  $p_{xx}$   $p_{yy}$  a, a, b and b of the unit cell labeled in Fig. 1(b), by considering a scale factor a with the values from 1 to 1.2 at a step of 0.05. Fig. 6(a) displays a set of top-view SEM images of the metasurfaces having the increased scale factors. The absorption spectra from the chiral metasurfaces are recorded with a Fourier transform infrared spectrometer, where a holographic wire grid linear polarizer and a zero order mid-infrared quarter-wave plate are used to generate the RCP and LCP incident light. The simulated and measured optical absorption spectra are presented in Fig. 6(b) and (c), respectively. It shows that the chiral plasmonic resonance of the metasurfaces redshifts continuously from 4.96 to 5.82  $\mu$ m as the scale factor a0.57 over this wavelength range. The maximum chiral light absorption achieved in experiment is 0.82 with the highest CD value of 0.62 for the metasurface of a1 at the chiral plasmonic



**Fig. 4.** (a) Distributions of electric field |E| (color map) and electric field vector E (black arrows) at the plane of x = 1000 nm for RCP and LCP incident light. (b) Distributions of magnetic field  $H_x$  (color map) and current density vector J (black arrows) at the plane of x = 1000 nm. (c) Distributions of Poynting Vector |P| (color map) and P (black arrows) at the plane of x = 1000 nm.



**Fig. 5.** (a) Simulated absorption spectra of the metasurfaces with different m and t = 65 nm for RCP light (color solid lines) and LCP light (color dashed lines). (b) Simulated absorption spectra of the metasurfaces with different t and m = 250 nm.

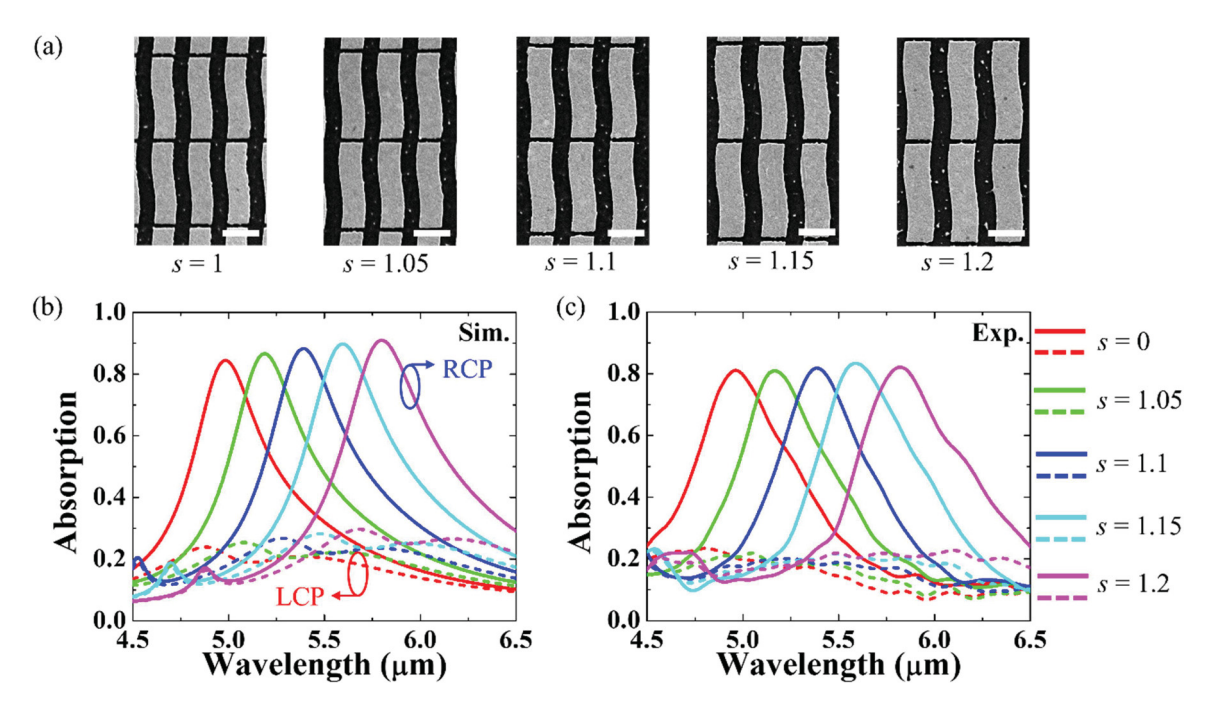


Fig. 6. (a) Top-view SEM images of the metasurfaces with increased scale factors. Scale bar: 2 μm. (b) Simulated and (c) experimental absorption spectra of the metasurfaces with increased scale factors for RCP light (color solid lines) and LCP light (color dashed lines).

#### resonance of 4.96 µm.

Furthermore, the degree of symmetry breaking for the wavy rectangle structure is adjusted by only varying the vertical shift of the cutting slot d, so that the CD value can be continuously tuned from positive to zero and negative without altering the chiral resonance wavelength. Fig. 7(a) shows a set of top-view SEM images of the metasurfaces with various vertical shifts of the cutting slot d increased from 0 to 2.4 µm, with the simulated and measured CD spectra plotted in Fig. 7(b) and (c). It is demonstrated that the maximum CD response is reached at d=0 with the CD value of 0.65 in simulation and 0.62 in experiment, where the degree of symmetry breaking for the wavy rectangle structure is the largest. As d is increased from 0 to 1.2 µm  $(p_y/4)$ , the CD value gradually decreases down to zero resulting from the reduced degree of symmetry breaking in the structure. As d is further increased from 1.2 to 2.4 µm  $(p_y/2)$ , CD is continuously switched from zero to negative values of - 0.65 in simulation and - 0.62 in experiment, caused by the increased degree of symmetry breaking in the structure. It is indicated that the chiral plasmonic resonance is almost unchanged as d is shifted due to the unique geometric symmetry properties of the wavy rectangle structure. The slight deviation between the simulated and measured CD spectra is potentially caused by the device defects introduced in the fabrication.

#### 3. Conclusion

Chiral metasurfaces of wavy rectangle resonators in mid-infrared frequencies have been studied with high and tunable CD values.

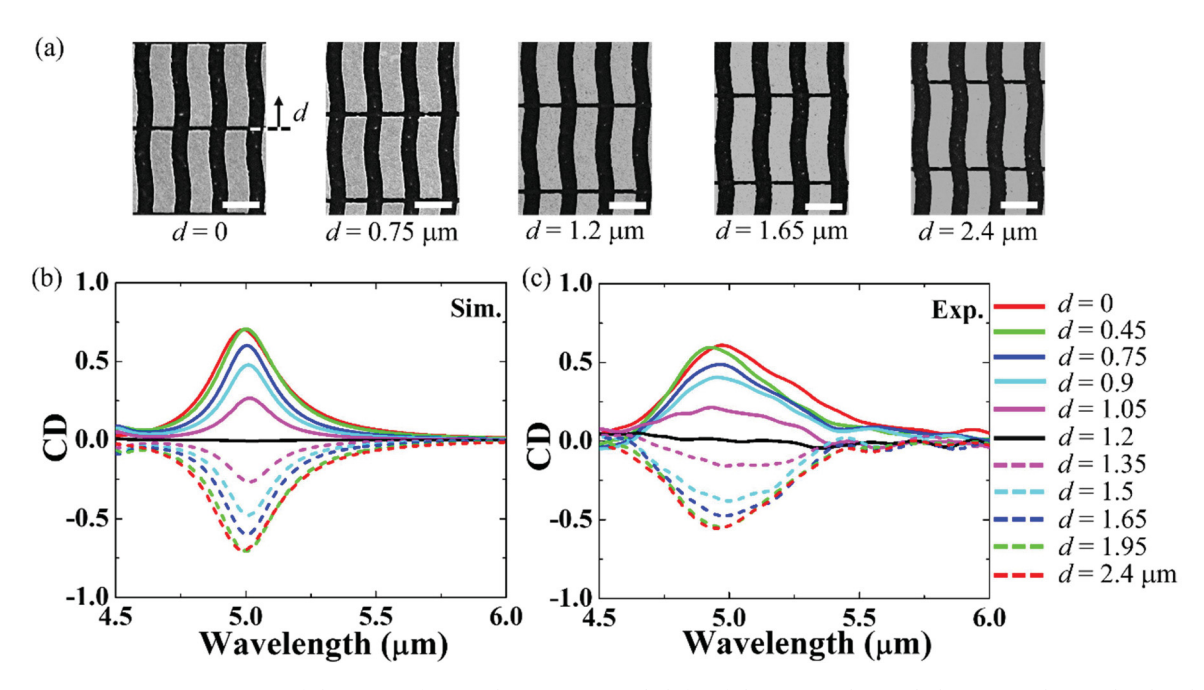


Fig. 7. (a) Top-view SEM images of the metasurfaces with various vertical shifts of the cutting slot. Scale bar: 2 μm. (b) Simulated and (c) experimental CD spectra of the metasurfaces with different vertical shifts of the cutting slot d from 0 to 2.4 μm.

The underlying mechanism of chiroptical response in the metasurface is explained with the electromagnetic field distributions of the chiral resonant modes. The chiral plasmonic resonance of the metasurface is tuned by linearly enlarging the geometric dimensions of the metasurface unit cell, while a high CD value is maintained. The chiroptical response of the metasurface can also be reduced, switched off or reversed by adjusting the location of the cutting slot to vary the degree of symmetry breaking for the wavy rectangle structure, where the CD value is continuously tuned from positive to zero and negative with the chiral resonance wavelength unchanged. Our results will advance many exciting applications in mid-infrared frequencies including protein molecule detection, infrared spectroscopy, thermal emission control, thermal radiation energy harvesting, and infrared-light communication.

## **Declaration of Competing Interest**

The authors declare that they have no known competing financial interests or personal relationships that could have appeared to influence the work reported in this paper.

#### Data Availability

Data will be made available on request.

#### Acknowledgements

The authors acknowledge support from the National Science Foundation, USA (Grant No. ECCS-2230071, ECCS-2230069 and ECCS-2204163). Work performed at the Center for Nanoscale Materials, a U.S. Department of Energy Office of Science User Facility, was supported by the U.S. DOE, Office of Basic Energy Sciences, under Contract No. DE-AC02-06CH11357. The authors also acknowledge the support from the Intelligent Systems Center and the facility support from the Materials Research Center at Missouri S&T.

#### References

- [1] S.S. Oh, O. Hess, Chiral metamaterials: enhancement and control of optical activity and circular dichroism, Nano Converg. 2 (2015) 1–14, https://doi.org/10.1186/s40580-015-0058-2.
- [2] X. Ma, M. Pu, X. Li, Y. Guo, P. Gao, X. Luo, Meta-chirality: Fundamentals, construction and applications, Nanomaterials 7 (2017) 116, https://doi.org/10.3390/nano7050116.
- [3] B. Sun, Y. Yu, Analysis of circular dichroism in chiral metamaterial at terahertz frequencies, J. Phys. D. 52 (2018), 025105, https://doi.org/10.1088/1361-6463/aaeaba.
- [4] X. Wang, Z. Tang, Circular dichroism studies on plasmonic nanostructures, Small 13 (2017), 1601115, https://doi.org/10.1002/smll.201601115.
- [5] J. Kästel, M. Fleischhauer, S.F. Yelin, R.L. Walsworth, Tunable negative refraction without absorption via electromagnetically induced chirality, Phys. Rev. Lett. 99 (2007), 073602, https://doi.org/10.1103/PhysRevLett.99.073602.

[6] S. Zhang, Y.S. Park, J. Li, X. Lu, W. Zhang, X. Zhang, Negative refractive index in chiral metamaterials, Phys. Rev. Lett. 102 (2009), 023901, https://doi.org/10.1103/PhysRevLett.102.023901.

- [7] Z. Li, M. Mutlu, E. Ozbay, Chiral metamaterials: from optical activity and negative refractive index to asymmetric transmission, J. Opt. 15 (2013), 023001, https://doi.org/10.1088/2040-8978/15/2/023001.
- [8] X. Zeng, D. Rosenmann, D.A. Czaplewski, J. Gao, X. Yang, Mid-infrared chiral metasurface absorbers with split-ellipse structures, Opt. Commun. 525 (2022), 128854, https://doi.org/10.1016/j.optcom.2022.128854.
- [9] Y. Cheng, H. Chen, J. Zhao, X. Mao, Z. Cheng, Chiral metamaterial absorber with high selectivity for terahertz circular polarization waves, Opt. Mater. Express 8 (2018) 1399–1409, https://doi.org/10.1364/OME.8.001399.
- [10] M. Li, L. Guo, J. Dong, H. Yang, An ultra-thin chiral metamaterial absorber with high selectivity for LCP and RCP waves, J. Phys. D. 47 (2014), 185102, https://doi.org/10.1088/0022-3727/47/18/185102.
- [11] A.Y. Zhu, W.T. Chen, A. Zaidi, Y.W. Huang, M. Khorasaninejad, V. Sanjeev, C.W. Qiu, F. Capasso, Giant intrinsic chiro-optical activity in planar dielectric nanostructures, 17158-17158, Light Sci. Appl. 7 (2018), https://doi.org/10.1038/lsa.2017.158.
- [12] C.M. Watts, X. Liu, W.J. Padilla, Metamaterial electromagnetic wave absorbers, Adv. Mater. 24 (2012) OP98–OP120, https://doi.org/10.1002/adma.201200674.
- [13] S. Jahani, Z. Jacob, All-dielectric metamaterials, Nat. Nanotechnol. 11 (2016) 23–36, https://doi.org/10.1038/nnano.2015.304.
- [14] C.R. Simovski, P.A. Belov, A.V. Atrashchenko, Y.S. Kivshar, Wire metamaterials: physics and applications, Adv. Mater. 24 (2012) 4229–4248, https://doi.org/10.1002/adma.201200931.
- [15] B. Tang, Z. Li, E. Palacios, Z. Liu, S. Butun, K. Aydin, Chiral-selective plasmonic metasurface absorbers operating at visible frequencies, IEEE Photon. Technol. Lett. 29 (2017) 295–298, https://doi.org/10.1109/LPT.2016.2647262.
- [16] L. Ouyang, W. Wang, D. Rosenmann, D. Czaplewski, J. Gao, X. Yang, Near-infrared chiral plasmonic metasurface absorbers, Opt. Express 26 (2018) 31484–31489, https://doi.org/10.1364/OE.26.031484.
- [17] Z. Li, D. Rosenmann, D. Czaplewski, X. Yang, J. Gao, Strong circular dichroism in chiral plasmonic metasurfaces optimized by micro-genetic algorithm, Opt. Express 27 (2019) 28313–28323, https://doi.org/10.1364/OE.27.028313.
- [18] Y. Lin, H. Guo, D. Che, J. Wang, Switchable plasmonic chirality for light modulation: from near-field to far-field coupling, J. Phys. Chem. Lett. 14 (2023) 1403–1410, https://doi.org/10.1021/acs.jpclett.2c03659.
- [19] H. Tang, D. Rosenmann, D.A. Czaplewski, X. Yang, J. Gao, Dual-band selective circular dichroism in mid-infrared chiral metasurfaces, Opt. Express 30 (2022) 20063–20075, https://doi.org/10.1364/OE.457218.
- [20] S. Mahmud, D. Rosenmann, D.A. Czaplewski, J. Gao, X. Yang, Chiral plasmonic metasurface absorbers in mid-infrared wavelength range, Opt. Lett. 45 (2020) 5372–5375, https://doi.org/10.1364/OL.404192.
- [21] S. Li, T. Sang, C. Yang, Y. Pei, Q. Mi, Y. Wang, G. Cao, C. Liu, Chiral metasurface absorbers with tunable circular dichroism in the mid-infrared via phase transition of vanadium dioxide, Opt. Commun. 521 (2022), 128557, https://doi.org/10.1364/OE.476021.
- [22] D.A. Therien, S.T. Read, S.M. Rosendahl, F. Lagugné-Labarthet, Optical resonances of chiral metastructures in the mid-infrared spectral range, Isr. J. Chem. (2022), 202200007, https://doi.org/10.1002/ijch.202200007.
- [23] Y. Hu, Y. Wang, T. Sang, G. Yang, Mid-infrared circular-polarization-sensitive photodetector based on a chiral metasurface with a photothermoelectric effect, Appl. Opt. 62 (9) (2023) 2292–2299, https://doi.org/10.1364/AO.486815.
- [24] S. Mahmud, D. Rosenmann, D.A. Czaplewski, J. Gao, X. Yang, Plasmon-phonon coupling between mid-infrared chiral metasurfaces and molecular vibrations, Opt. Express 28 (2020) 21192–21201, https://doi.org/10.1364/OE.397725.
- [25] S. Yoo, Q.H. Park, Metamaterials and chiral sensing: a review of fundamentals and applications, Nanophotonics 8 (2019) 249–261, https://doi.org/10.1515/nanoph-2018-0167.
- [26] K.T. Lee, B. Kim, L. Raju, S.P. Rodrigues, D.H. Ko, W. Cai, Enantiomer-selective molecular sensing in the nonlinear optical regime via upconverting chiral metamaterials, Adv. Funct. Mater. 32 (2022), 2208641, https://doi.org/10.1002/adfm.202208641.
- [27] T. Ullah, A. Rashid, Angularly stable and broadband chiral metamaterial based design for asymmetric transmission of linearly polarized waves, Microw. Opt. Technol. Lett. 63 (1) (2021) 226–234, https://doi.org/10.1002/mpp.32564.
- [28] P. Ding, E. Liang, G. Cai, W. Hu, C. Fan, Q. Xue, Dual-band perfect absorption and field enhancement by interaction between localized and propagating surface plasmons in optical metamaterials, J. Opt. 13 (7) (2011), 075005, https://doi.org/10.1088/2040-8978/13/7/075005.
- [29] J.A. Mason, G. Allen, V.A. Podolskiy, D. Wasserman, Strong coupling of molecular and mid-infrared perfect absorber resonances, IEEE Photon. Technol. Lett. 24 (1) (2011) 31–33, https://doi.org/10.1109/LPT.2011.2171942.
- [30] Y. Li, L. Su, C. Shou, C. Yu, J. Deng, Y. Fang, Surface-enhanced molecular spectroscopy (SEMS) based on perfect-absorber metamaterials in the mid-infrared, Sci. Rep. 3 (1) (2013) 2865, https://doi.org/10.1038/srep02865.
- [31] L.A. Warning, A.R. Miandashti, L.A. McCarthy, Q. Zhang, C.F. Landes, S. Link, Nanophotonic approaches for chirality sensing, ACS Nano 15 (10) (2021) 15538–15566. https://doi.org/10.1021/acsnano.1c04992.
- [32] P. Banzer, P. Woźniak, U. Mick, I. De Leon, R.W. Boyd, Chiral optical response of planar and symmetric nanotrimers enabled by heteromaterial selection, Nat. Commun. 7 (1) (2016) 13117, https://doi.org/10.1038/ncomms13117.
- [33] D.A. Therien, S.T. Read, S.M. Rosendahl, F. Lagugné-Labarthet, Optical resonances of chiral metastructures in the mid-infrared spectral range, Isr. J. Chem. (2022), 202200007, https://doi.org/10.1002/ijch.202200007.
- [34] J. Fan, T. Lei, X. Yuan, Tunable and reconfigurable dual-band chiral metamirror, IEEE Photon. J. 12 (5) (2020) 1–8, https://doi.org/10.1109/ JPHOT.2020.3020090.
- [35] J. Kischkat, S. Peters, B. Gruska, M. Semtsiv, M. Chashnikova, M. Klinkmüller, O. Fedosenko, S. Machulik, A. Aleksandrova, G. Monastyrskyi, Mid-infrared optical properties of thin films of aluminum oxide, titanium dioxide, silicon dioxide, aluminum nitride, and silicon nitride, Appl. Opt. 51 (2012) 6789–6798, https://doi.org/10.1364/AO.51.006789.
- [36] A.D. Rakić, A.B. Djurišić, J.M. Elazar, M.L. Majewski, Optical properties of metallic films for vertical-cavity optoelectronic devices, Appl. Opt. 37 (1998) 5271–5283, https://doi.org/10.1364/AO.37.005271.